Mesoscale Shape Memory Alloy Actuator for Visual Clarity of Surgical Cameras in Minimally Invasive Robotic Surgery

Xiaolong Liu, *Member, IEEE*, Hui Liu, and Jindong Tan, *Member, IEEE*

***Abstract*—This paper proposes a mesoscale shape memory alloy (SMA) actuator for cleaning the contaminated lenses of surgical cameras during minimally invasive robotic surgery. The proposed design features minimal intraopertive interruption to maintain visual clarity of fully insertable surgical cameras by quickly removing vapor condensation, particle debris, body fluids, etc. that adhere to the cover lenses. Inspired by the mechanical properties of 1-D SMA materials, a set of SMA wires are employed to drive an eyelid wiper that is concealed in the module's edge. By analyzing the actuation mechanism, we provide a design guideline for developing a functional modular actuator. A numerical computation model is also proposed to predict the actuation cycles according to various combinations of design parameters. The performance of an initial prototype is experimentally evaluated by introducing three different contamination sources, i.e., fogging, bone dusts, and blood. The predicted actuation cycle is experimentally validated with 95.2% prediction accuracy. And the actuation cycle of the eyelid wiper is about 2 s.**

***Index Terms*—SMA actuator, robotic surgery, lens cleaning, clear vision.**

I. Introduction

CLEAR visualization of the surgical field in minimally invasive surgery (MIS) is vitally important for the surgeon's operation efficiency and the patient's safety. Surgical scope cameras were developed with various dimensions, flexibility, and controllability to reach the anatomies inside human bodies for various types of MIS, such as laparoscopic, endoscopic, and thoracoscopic [1], etc. Surgeons manipulate surgical instruments to carry out surgical procedures solely based on the visual guidance of these scope cameras. Uninterrupted and clear visual guidance is critical to the success of all these surgeries. However, clarity of the visual field of surgical scope cameras can easily get impaired by contaminated lenses because of vapor condensation [2], particle debris, rinsing fluid, and body fluids [3]. According to clinical investigation, more than 37% of laparoscopic surgery time is done with impaired rigid laparoscopes [4] due to contamination of camera lenses that is considered troublesome by 68% surgeons [5], which increases the procedure length and surgery cost. More seriously, the distraction may affect surgeons' judgment, and cause patient injury [6]–[8]. A visually impaired rigid laparoscope could be externally cleaned with low efficiency. Nevertheless, this situation for flexible scope cameras which reach deep inside body cavity or for remotely controlled robotic cameras could be catastrophic for both patients and surgeons.

With the tremendous success of rigid laparoscopes in MIS, growing attention has been drawn for improving impaired vision during surgery. The common solution to the cleaning of rigid laparoscopes is to remove them from the body cavity and wipe up the contaminated lenses externally [3], which significantly interrupts the surgical flow, reduces surgeons' operation efficiency and potentially jeopardizes patient's safety. Though chemical coatings with hydrophobicity and/or lipophobicity can alleviate camera lenses to be contaminated by fogging and/or viscous body fluid [9], more reliable lens cleaning methods are demanded. By deploying wiping stations such as extendable swab devices [10] or wiping sleeves [11], [12] in the body cavity, the camera lenses of laparoscopes can be redirected to interaction with the wiping stations. Laparoscopic cannulas with swabs installed at the distal ends were developed for lens cleaning by initiating axial reciprocating stroke of laparoscopes [13], [14]. Alternatively, rinsing fluid or gas (carbon dioxide) flows can be guided through a laparoscope's overtube [15], [16] for flushing off contaminants on the camera's cover lens. In summary, these laparoscope-delicated solutions are either requiring camera motion that can still interrupt ongoing surgical procedure, or demanding external pressor devices for delivering fluid/gas that significantly complicates the whole system. Moreover, challenges will arise when the solutions apply to fully insertable cameras or flexible cameras due to their unique forms, operating procedures, and control methods. There is a need of developing a clear vision mechanism that can be applied to various forms of surgical cameras with minimal intraoperative visual interruption.

This paper takes on the critical challenge to make an initial step towards this goal. We present an innovative mesoscale modular clear vision system (refer to as vClear system) to mimic mammalian eyelids [17] for cleaning contaminated cover lenses of the fully insertable robotic camera developed in our prior research [18]. The robotic camera features optimized illumination that addresses inferior lighting uniformity

Manuscript received May 21, 2019; revised July 17, 2019; accepted July 18, 2019. Date of publication July 24, 2019; date of current version August 21, 2019. This paper was recommended for publication by Associate Editor P. Poignet and Editor P. Dario upon evaluation of the reviewers' comments. *(Corresponding author: Xiaolong Liu.)*

The authors are with the Department of Mechanical, Aerospace and Biomedical Engineering, University of Tennessee, Knoxville, TN 37996 USA (e-mail: xliu57@vols.utk.edu).

Digital Object Identifier 10.1109/TMRB.2019.2930752

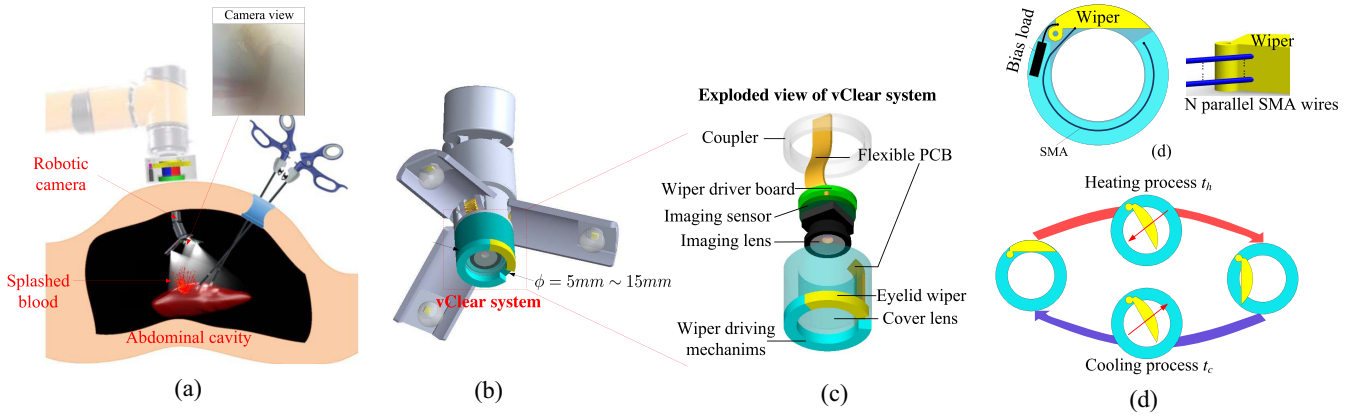

Fig. 1. Conceptual illustration of the vClear system. (a) Blurred vision of an insertable surgical camera by splashed blood. (b) Integrating the vClear system in our surgical camera. (c) The exploded view of the vClear system. (d)-(e) Working principle of the eyelid wiper actuation mechanism.

and low optical efficiency in the state-of-the-art designs of *in vivo* laparoscopic cameras. Fig. 1a demonstrates the scenario that the vision of the robotic camera is impaired by splashed blood. Instead of employing electrical motors to drive design-dependent mechanical wipers for insertable surgical cameras [19], the vClear system, as shown in Fig. 1b, is with an appearance of a sealing cover to encompass the camera module. The vClear system consists of four major components shown in Fig. 1c-d: an eyelid-like wiper concealed in the module's edge; a cornea-like cover lens for sealing the camera lens and imaging sensors; a set of shape memory alloy (SMA) wires for mimicking muscles to actuate the eyelid wiper; and an anodized aluminum alloy structure to support the above components. During surgical procedure, the eyelid wiper is activated to blink off contaminants on the cover lens.

The research challenge on developing such a mesoscale vClear system is twofold: (1) confining the eyelid wiper in small space and delivering sufficient energy for the lens cleaning; and (2) enabling rapid wiping cycle for minimal intraoperative visual interruption. Miniature actuators based on piezoelectric materials (PZTs), electroactive polymers (EAPs), and SMAs suffer actuation performance trade-off between deformation, output forces, and actuation frequencies. Piezoelectric bending actuators feature highest actuation frequency at kHz scale [20], but they are limited by their small deflections and light actuation force. EAP actuators can achieve large recoverable strains (40%$\sim$ 900%) and large output force [21]. However, the high voltages ($>$1 kV) are required to activate EAP actuators for obtaining such performance [22]. SMA materials features high power-to-weight ratio, low driving voltages, 4%$\sim$8% recoverable strains, and great biocompatibility. Compared with PZT actuators, the main limitation of SMA actuators is their lower actuation frequencies (0.1 Hz$\sim$35 Hz) [23]. Fortunately, this range of actuation frequency is sufficient for the eyelid wiper design (cleaning the contaminated lens within seconds).

The design of an effective actuation mechanism for the eyelid wiper involves considering the SMA wires' internal stress changes during phase transformation, bias stresses, and the wiping friction between the eyelid wiper and the cover lens. The actuation cycle of the eyelid wiper is determined by the strain rates of SMA wires which are influenced by the bias stress, heat convection coefficient, and Joule heating strategy [24]. The modeling of actuation cycles based on these factors is necessary to assist in designing the vClear system.

The primary research contributions of this paper include: (1) designing a mesoscale clear vision module based on one-dimensional SMA materials for our insertable robotic camera system, and providing actuation mechanism analysis and design guideline for the modular actuator; (2) developing a numerical model to predict the actuation cycles according to various combinations of design parameters; and (3) experimentally validating the actuation cycle prediction model and demonstrating the efficiency of cleaning the contaminated cover lens of the surgical camera.

II. Conceptual Design and Working Principle

The schematic of the modularized vClear system is illustrated in Fig. 1d. A miniature eyelid wiper is connected with N paralleled SMA wires that are embedded in the module's circular edge. A bias load connects to the wiper on the outer side of the pivot hinge, and provides force to reset the wiper's position after being actuated by the SMA wires.

The working principle of the eyelid wiper mechanism involves controlling the SMA wires' material phase by Joule heating. An SMA wire has two distinct phases including the high temperature phase (austenite A) and the low temperature phase (martensite M). When an elongated SMA wire (at the phase of detwinned martensite M_d) is heated above its austenite finish temperature A_f, the wire contracts to recover its original shape (at the phase of A) by the activated internal driving energy which is capable of overcoming certain bias load [25]. When the wire is cooled from A_f to the martensite finish temperature M_f under the condition of zero-load, the wire transforms to the phase of twinned martensite M_t with unnoticeable macroscale length change. Upon applying bias load to the wire, it can transform from M_t to M_d, which induces the wire's elongation.

Fig. 1e demonstrates a full actuation cycle of the eyelid wiper mechanism. In the heating process, the SMA wires

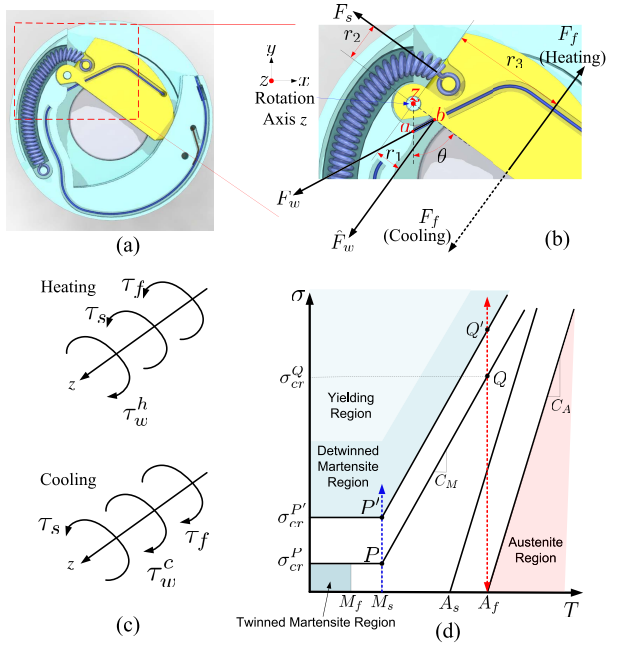

Fig. 2. Design and analysis of the eyelid wiper actuation mechanism. (a) vClear system design illustration; (b) Schematic of actuation mechanism; (c) Torque analysis; (d) Critical stresses for phase transformation of SMA wires. M_f, M_s, A_s, A_f are phase transformation temperatures under zero stress. C_M and C_A are stress influence coefficients.

transform from M_d to A, which results in contractive deformation of the wires, and consequently drives the wiper to sweep across the cover lens. In the cooling process, the SMA wires are tensioned by the bias load, and transform from A to M_d. The eyelid wiper can thus be pulled back to its initial position.

The bias load can come with various types, such as constant force spring, extensions spring, magnets or even another set of SMA wires. By considering the design and manufacturing simplicity, we employ a micro extension spring as the bias load for the eyelid wiper mechanism. However, a stiff spring may apply excessive bias force that blocks the contraction of SMA wires during the heating process. While a soft spring may provide insufficient bias force to reset the eyelid wiper. In the following section, we analyze the actuation mechanism and propose a method to guarantee a functional design.

III. Quasi-Static Actuation Analysis

A. Force Bounds of Micro Extension Spring

Fig. 2a shows the design configuration of a proof-of-concept vClear system. The actuation of the eyelid wiper involves the torques of $\tau_w = \hat{F}_w r_1$ from the SMA wires, $\tau_s = F_s r_2$ from the micro extension spring, and $\tau_f = F_f r_3$ from the friction between the wiper and the cover lens, as shown in Fig. 2b. By assuming that the actuation mechanism works in a quasi-static manner, the heating and cooling processes are governed by equations in (1), and illustrated in Fig. 2c.

$$\underbrace{\frac{r_1}{r_2}\hat{F}_w^h - \frac{r_3}{r_2}F_f = F_s}_{F_U \text{ in Heating}}, \quad \underbrace{\frac{r_1}{r_2}\hat{F}_w^c + \frac{r_3}{r_2}F_f = F_s}_{F_L \text{ in Cooling}}, \tag{1}$$

where $\hat{F}_w^h$ and $\hat{F}_w^c$ are effective SMA forces during heating and cooling processes respectively; $F_f = \mu F_N$; μ denotes frictional coefficient between the wiper and the cover lens; F_N is the applied force on the cover lens from the wiper. If the bounds of the actuation forces F_U and F_L can be calculated for the spring force $F_s \in [F_L, F_U]$ which is a function of the wiper's rotational angle θ and modeled in (2), the spring rate k and the initial tension F_i of an extension spring can be selected accordingly. ΔL represents the length deformation when $\theta = \pi/2$.

$$F_s(\theta) = k\left(r_2\left(\frac{\pi}{2} - \theta\right) + \Delta L\right) + F_i. \tag{2}$$

B. Force of SMA Wires

The effective force $\hat{F}_w$ from the SMA wires is modeled as

$$\hat{F}_w = N\sigma S_c \cos\left(\frac{\theta}{2}\right), \tag{3}$$

where N is the number of SMA wires that drive the wiper; σ and $S_c = \pi(d/2)^2$ denote the wires' internal stress and cross sectional area. d represents the wire diameter. According to (1), the bound of F_s can be determined by using $\hat{F}_w^h$ and $\hat{F}_w^c$. The SMA wire stress σ is the key variable in $\hat{F}_w$. The boundary values of σ are needed to determine F_U and F_L for the heating and cooling processes.

Fig. 2d shows the critical stress model of one-dimensional SMAs for phase transformation [26]. The $\sigma - T$ graph indicates that it requires increasing applied stresses for SMA wires to transform to M_d when $T > M_s$, and nearly constant applied stress for SMA wires to transform to M_d when $T < M_s$. In the heating process, when $T = A_f$ (the austenite finish temperature under zero stress), the SMA wires exhibits the property of superelasticity shown in the red arrows. When the bias stress increases above σ_{cr}^Q, the SMA wires will start to be elongated and fail in actuating the wiper. In the cooling process, when the SMA wires cools down to $T = M_s$ (the martensite start temperature under zero stress), the bias stress needs to provide at least $\sigma_{cr}^{P'}$ on the SMA wires in addition to overcome the friction for resetting the wiper to its initial position. The critical stress σ_{cr}^Q can be calculated by

$$\sigma_{cr}^Q = \sigma_{cr}^P + C_M(A_f - M_s), \tag{4}$$

where σ_{cr}^P, C_M, A_f, M_s, and $\sigma_{cr}^{P'}$ are all material-related parameters. σ_{cr}^Q and $\sigma_{cr}^{P'}$ can be used to determine $\hat{F}_w^h$ and $\hat{F}_w^c$ respectively according to (3).

IV. Actuation Cycle Modeling and Prediction

A full actuation cycle (or strain cycle) time of the eyelid wiper adds up durations of the heating process t_h and the cooling process t_c, as shown in Fig. 1e. The strain ϵ of one SMA wire is represented by $\epsilon = L_{ab}/L$, where L_{ab} is the length between the points a and b in Fig. 2b; and L denotes the length of the SMA wire. The strain ϵ continuously changes between 0 (when $\theta = 0$) and ϵ_L (when $\theta = \pi/2$) in each cycle. The objective of this section is to estimate strain cycle periods for the eyelid wiper mechanism according to various design parameters.

A. System of First Order Differential Equations

The strain rate $\dot{\epsilon}$ of an SMA wire is determined by the cycle time of material phase transformation, which is governed by the one-dimensional constitutive equation of SMAs [26]

$$\dot{\sigma} = D\dot{\epsilon} + \Omega\dot{\xi} + \Theta\dot{T}, \tag{5}$$

where D is the Young's modulus; Ω is transformation tensor; ϵ is the wire strain; ξ is martensite fraction; Θ is the thermal expansion coefficient; and T is the wire temperature. The term $\Theta\dot{T}$ is ignorable due to the small value of Θ. The martensite fraction ξ that characterizes the phase transformation kinetics can be modeled as $\xi_h = f_{\xi_h}(\sigma_h, T)$ for $M_d \rightarrow A$ and $\xi_c = f_{\xi_c}(\sigma_c, T)$ for $A \rightarrow M_d$ in (6) and (7)

$$\xi_h = \frac{1}{2}\cos\left\{a_A\left(T - A_s - \frac{\sigma}{C_A}\right)\right\} + \frac{1}{2}, \tag{6}$$

$$\xi_c = \frac{1}{2}\cos\left\{a_M\left[\sigma - \sigma_{cr}^{P'} - C_M(T - M_s)\right]\right\} + \frac{1}{2}, \tag{7}$$

where $a_A = \pi/(\sigma_{cr}^{P} - \sigma_{cr}^{P'})$ and $a_M = \pi/(A_f - A_s)$. According to (1), (3) and the system configuration in Fig. 2b, σ can be modeled as $\sigma_h = f_{\sigma_h}(\epsilon)$ for $M_d \rightarrow A$, and $\sigma_c = f_{\sigma_c}(\epsilon)$ for $A \rightarrow M_d$, which are detailed in Section IV-B. By taking the derivative of σ and ξ in respect to time t and substituting $\dot{\sigma}$, $\dot{\xi}$ in (5), the constitutive equation is reformulated as a first order differential equation with variables ϵ and T

$$f'_{\sigma_\square}(\epsilon, \dot{\epsilon}) = D\dot{\epsilon} + \Omega f'_{\xi_\square}\left(f_{\sigma_\square}(\epsilon), f'_{\sigma_\square}(\epsilon, \dot{\epsilon}), T, \dot{T}\right), \tag{8}$$

where the subscript $\square$ denotes h for the heating process and c for the cooling process.

To solve the strain cycle time, another set of $\epsilon - T$ relation is required. From the perspective of energy balance for SMA wires, the rate of heat flow is approximately equal to the rate of energy change when the ratio of wire length and diameter is sufficiently large (biot number $B_i < 0.1$) [27]. Thus, the heat transfer equation of an SMA wire can be formulated by

$$mc_p\dot{T} - m\Delta h\dot{\xi}_\square = I^2R + \dot{E}, \tag{9}$$

where m is the wire mass; c_p is specific heat in constant pressure; Δh is the latent heat of transformation; I is the input current and equals to zero during the cooling process; R is the electrical resistance; and E represents the heat energy in the SMA wire.

In many applications, SMA wires are exposed in the air or submerged in heat dissipation liquids, which enable $\dot{E}$ to be formulated by directly using the heat convection model. However, the SMA wires in our design are embedded in the aluminum structure. The heat energy of the SMA wires will flow into the structure by conduction, and then go into the surrounding air by convection. To eliminate the air layer between the SMA wire and the aluminum structure, thermal grease is employed to fill the air gap. When the thickness of the thermal grease is small enough, the conduction term for such a layer is negligible. In our design, the thickness of the thermal grease layer is about 10 μm. This value is far less than the thickness of the aluminum structure Δr (see Table II). Therefore, we model $\dot{E}$ based on these two steps.

The thermal energy in the SMA wires equals to the amount of heat energy transferred from the surrounding structure to the wires by heat conduction.

$$\dot{E} = k_a S_a \frac{T_a - T}{\Delta r}, \tag{10}$$

where k_a is the thermal conductivity of the structure; S_a is the surface area of the SMA wire; Δr represents the distance between the center of SMA wires and the equivalent middle circle of the surrounding structure; and T_a is the surrounding structure temperature.

The thermal energy stored in the surrounding structure equals to the amount of conductive heat from the SMA wires plus the amount of heat transfer by convection from the surrounding environment.

$$m_a c_{p_a}\dot{T}_a = -k_a S_a \frac{T_a - T}{\Delta r} - hS_b(T_a - T_\infty), \tag{11}$$

where m_a is the structure mass; c_{p_a} is the structure specific heat; h is the heat convection coefficient; S_b represents the area of the structure surface in contact with the surrounding air; and T_∞ is the ambient temperature.

By substituting $\dot{\xi}_\square = f'_{\xi_\square}(f_{\sigma_\square}(\epsilon), f'_{\sigma_\square}(\epsilon, \dot{\epsilon}), T, \dot{T})$ in (9), we can derive the extra $\epsilon - T$ relation in the form of first order differential equation. The unknown parameter T_a in (9) can be simultaneously solved by (11).

B. Modeling of $\sigma_\square = f_{\sigma_\square}(\epsilon)$

By combining (1), (2), and (3), the relations of σ and θ for the heating and cooling processes are obtained. To formulate $\sigma_\square = f_{\sigma_\square}(\epsilon)$, we need to replace θ with ϵ. θ and $\cos(\theta/2)$ in (2) and (3) can be formulated as functions of ϵ by using the law of cosines

$$\theta = \arccos\left(\frac{L_{za}^2 + L_{zb}^2 - \epsilon^2 L^2}{2L_{za}L_{zb}}\right), \tag{12}$$

$$\cos\left(\frac{\theta}{2}\right) = \sqrt{\frac{1}{2} + \frac{L_{za}^2 + L_{zb}^2 - \epsilon^2 L^2}{4L_{za}L_{zb}}}, \tag{13}$$

where L_{za} and L_{zb} are the lengths of $z - a$ and $z - b$, as shown in Fig. 2b. However, considering that $\sigma_\square = f_{\sigma_\square}(\epsilon)$ and $\dot{\sigma}_\square = f'_{\sigma_\square}(\epsilon, \dot{\epsilon})$ will be used in (8) and (9), the nonlinearity of (12) and (13) can significantly increase the complexity of (8) and (9) that leads to uncoverged numerical computation for ϵ and T. To address this problem, we employ second and third degree polynomial functions to reformulate (12) and (13) for reducing their nonlinearity in (14) and (15)

$$\theta(\epsilon) = \sum_{m=1}^{3} p_m \epsilon^{3-m}, \tag{14}$$

$$\cos\left(\frac{\theta}{2}\right) = \sum_{n=1}^{4} q_n \epsilon^{4-n}, \tag{15}$$

where p_m and q_n ($m = 1, 2, 3$, $n = 1, 2, 3, 4$) are polynomial coefficients. $\sigma_\square = f_{\sigma_\square}(\epsilon)$ can thus be formulated by using (1), (2), (3), (14), and (15) as

$$\sigma_\square = f_{\sigma_\square}(\epsilon) = \frac{G - kr_2^2 \sum_{m=1}^{3} p_m \epsilon^{3-m} + r_3 \hat{F}_f}{r_1 N S_a \sum_{n=1}^{4} q_n \epsilon^{4-n}}, \tag{16}$$

where $G = \pi k r_2^2/2 + k r_2 \Delta L + r_2 F_i$; $\hat{F}_f = F_f$ in the heating process and $\hat{F}_f = -F_f$ in the cooling process. The derivative of σ in (16) is defined as

$$\dot{\sigma}_\square = g_\square(\epsilon)\dot{\epsilon}, \tag{17}$$

where $g_\square(\epsilon)$ represents a function of ϵ.

C. Solving ϵ and T in Respect to t

The rate forms of ξ in (6) and (7) are derived as functions of ϵ and T by using (16) and (17), and represented by

$$\dot{\xi}_\square = w_\square(\epsilon, T)\dot{T} - u_\square(\epsilon, T)\dot{\epsilon}, \tag{18}$$

where

$$w_h = -\frac{a_A}{2}\sin\left[a_A(T - A_s) - \frac{a_A}{C_A}\sigma_h(\epsilon)\right], \tag{19}$$

$$w_c = \frac{a_M C_M}{2}\sin\left\{a_M\left[\sigma_c(\epsilon) - \sigma_{cr}^{P'} - C_M(T - M_s)\right]\right\}, \tag{20}$$

$$u_h = -\frac{a_A g_h(\epsilon)}{2C_A}\sin\left[a_A(T - A_s) - \frac{a_A}{C_A}\sigma_h(\epsilon)\right], \tag{21}$$

$$u_c = \frac{a_M g_c(\epsilon)}{2}\sin\left\{a_M\left[\sigma_c(\epsilon) - \sigma_{cr}^{P'} - C_M(T - M_s)\right]\right\}. \tag{22}$$

By substituting (18) and (17) for $\dot{\xi}$ and/or $\dot{\sigma}$ in (8) and (9), $\dot{\epsilon}$ and $\dot{T}$ are formulated as functions of ϵ and T in (23) and (24) with (25) for solving T_a

$$\dot{\epsilon} = \frac{\Omega w_\square\left(I^2R + k_a S_a(T_a - T)/\Delta r\right)}{\left(mc_p - m\Delta h w_\square\right)(g_\square - D + \Omega u_\square) + m\Delta h \Omega w_\square u_\square}, \tag{23}$$

$$\dot{T} = \frac{(g_\square - D + \Omega u_\square)\left(I^2R + k_a S_a(T_a - T)/\Delta r\right)}{\left(mc_p - m\Delta h w_\square\right)(g_\square - D + \Omega u_\square) + m\Delta h \Omega w_\square u_\square}, \tag{24}$$

$$\dot{T}_a = \frac{-(k_a S_a + hS_b\Delta r)T_a + (k_a S_a T + h\Delta r S_b T_\infty)}{m_a c_{p_a}\Delta r}. \tag{25}$$

The numerical computation of $\epsilon(t)$ and $T(t)$ involves determinating design parameters and initial conditions, and employing an effective numerical solver. The SMA property parameters including $M_f, M_s, A_s, A_f, C_M, C_A, c_p, h, D, \Omega$, etc., are provided by materials' datasheet or can be determined by running a set of testing experiments for the selected SMA wires. Compatible extension spring parameters k, F_i are obtained according to Section III. The proposed strain cycle model in (23), (24) and (25) can be treated as initial value problem (IVP) with initial conditions of $\epsilon_0 = \epsilon_L$ and $T = T_\infty$. Considering the nonlinearity of (23), (24), and (25), the fourth-order Runge-Kutta method [28] is employed as the numerical solver to approximate the solution of $\epsilon(t)$ and $T(t)$. The computed strain cycle is used to identify the actuation frequency of the eyelid wiper mechanism, and to optimize the design parameters for achieving faster actuation speeds.

V. Experiments

In this section, a prototype design of the vClear system is presented to integrate in the insertable robotic camera developed in our prior work [18] for the purpose of proof-of-concept. By elaborating the materials and parameters in Section V-A, we design the spring rates k and the initial tensions F_i of micro extension springs for effective actuation of the eyelid wiper according to the quasi-static analysis developed in Section III. The actuation cycles of the eyelid wiper are numerically computed based on various configurations of SMA wires and extension springs. We fabricate a prototype and evaluate the predicted actuation cycles by experiments. At last, the contaminant removal efficiency of the vClear system is evaluated by using the conditions of fogging, bone dusts, and blood.

TABLE I
Material Properties and Design Dimensions

Parameters	Value
Martensite finish temperature M_f (°C)	22.1
Martensite start temperature M_s (°C)	41.4
Austenite start temperature A_s (°C)	50.6
Austenite finish temperature A_f (°C)	68.1
Stress influence coefficient C_M (MPa°C^{-1})	6.05
Stress influence coefficient C_A (MPa°C^{-1})	14.25
Young's modulus at 100%austenite D_A (GPa)	71.7
Young's modulus at 100%martensite D_M (GPa)	12.5
Critical stress σ_{cr}^{P} (MPa)	50.6
Critical stress $\sigma_{cr}^{P'}$(MPa)	120.3
Maximum recoverable strain ϵ_L	0.045
Wiper-lens friction coefficient μ	0.4

A. Materials and Parameters

To design the proposed vClear system and analyze its performance, the initial step is to identify the design materials as well as the related material parameters.

1) SMA Wires: In this work, we employ a set of commercially available SMA wires (HT Flexinol Ni-Ti, Dynalloy Inc.) with diameters of 100 µm, 150 µm, 200 µm, 250 µm, 300 µm, and 375 µm for measuring the mechanical properties undisclosed by the datasheet [29], such as transformation temperatures under zero-stress M_f, M_s, A_s, A_f, Young's moduli D_A (at the phase of A) and D_M (at the phase of M_t), the maximum recoverable strain ϵ_L, and critical stresses σ_{cr}^{P} and $\sigma_{cr}^{P'}$. The measured parameters are summarized in Table I.

2) Cover Lens: The material of the cover lens adopts K9 crystal glass which features 99.4% visible light transmittance. Hydrophobic coating is applied to the external surface of the cover lens that enables the eyelid wiper to remove contaminants with ease.

3) Eyelid Wiper: The eyelid wiper combines two materials: anodized aluminum alloy for holding the SMA wires, and ethylene propylene diene monomer (EPDM) rubber with added polytetrafluoroethylene (PTFE). The employed rubber material is able to achieve low contact friction with cover lens ($\mu = 0.4$). The eyelid wiper applies about $F_N = 0.3$ N force against the cover lens. The friction force is estimated as $F_f = 0.12$ N.

4) Modular Structure: In consideration of our robotic camera's dimensions, the external diameter of the structure is limited at $\phi = 16$ mm. Three major functions are provided by the structure: (1) holding the cover lens in the front of the camera's imaging lens; (2) pairing with the eyelid wiper for its rotational motion; and (3) concealing the SMA wires at

TABLE II
ACTUATION CYCLE MODEL PARAMETERS

Parameters	Value
k_a Thermal conductivity of 6061 aluminum alloy (W/m-K)	205
m_a Mass of aluminum structure (g)	2.5
m Mass of SMA wires (mg)	4.3
c_{p_a} Specific heat of aluminum (J/kg-K)	896
c_p Specific heat of SMA (J/kg-K)	837
S_a Surface area of SMA wires (mm^2)	17.8
S_b Surface area of aluminum structure (mm^2)	351.8
R_A SMA electrical resistivity at austenite (Ωm)	8×10^{-7}
R_M SMA electrical resistivity at martensite (Ωm)	1×10^{-6}
Δh SMA latent of heat transformation (J/kg)	2.42×10^{4}
N Number of SMA wires	2
h Heat convection coefficient of air (W/m^2-K)	80
Δr Distance between centers of SMA and structure (mm)	2
T_∞ Ambient temperature (°C)	23
ϕ Module diameter (mm)	16
r_1 Lever arm length of SMA wires (mm)	1.2
r_2 Lever arm length of spring (mm)	1.64
r_3 Lever arm length of eyelid wiper (mm)	5.23

the structure's edge for actuating the eyelid wiper. The material of the structure is the identical aluminum alloy 6061 used for manufacturing the eyelid wiper. The structural dimensions such as the lever arms r_1, r_2, and r_3 are presented in Table II. The aluminum parts are anodized for electrical insulation of the embedded SMA wires.

5) Thermal Sensor: The phase transformation of SMA wires associates with temperature change. To control the Joule heating for actuating the eyelid wiper, we integrate a micro thermistor (Fμ3122-07U015, Semitec USA Corp.) in the vClear system for providing thermal feedback, as illustrated in Fig. 5c.

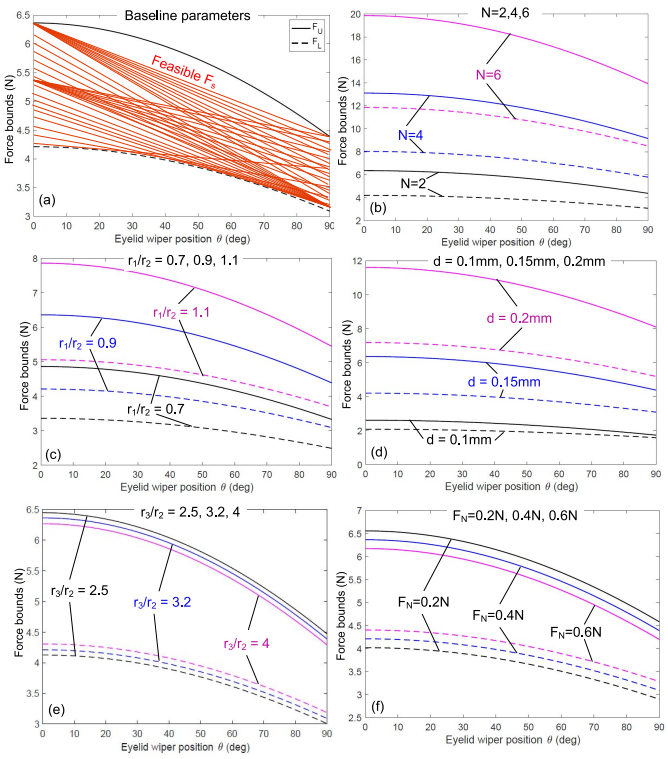

Fig. 3. Computed bounds of the micro spring force $F_s(\theta)$ based on various design parameters. (a) Demonstration of force bounds and feasible $F_s(\theta)$ according to the baseline parameters. (b) Varying SMA wire number $N = 2, 4, 6$. (c) Varying ratio of r_1 and r_2, $r_1/r_2 = 0.7, 0.9, 1.1$. (d) Varying the SMA wire diameter $d = 0.1\,\text{mm}, 0.15\,\text{mm}, 0.2\,\text{mm}$. (e) Varying ratio of r_3 and r_2, $r_3/r_2 = 2.5, 3.2, 4$. (f) Varying the eyelid wiper contact force $F_N = 0.2\,\text{N}, 0.4\,\text{N}, 0.6\,\text{N}$.

B. Micro Extension Spring Parameter Design

The design of micro extension springs for the vClear system is governed by the force bounds in (1). We investigate how the factors including $N, S_a, r_1, r_2, r_3, \mu, F_N$ impact on the design of micro extension springs. A set of baseline values are initially assigned to these parameters: $N = 2, d = 0.15\,\text{mm}, r_1/r_2 = 0.9, r_3/r_2 = 3.2, F_N = 0.4\,\text{N}$. By varying each parameter, the force bounds of $F_s(\theta)$ are computed by using the data in Table I, and are illustrated in Fig. 3.

Fig. 3a illustrates the force bounds computed with the baseline parameters. The solid black line represents the upper force bound F_U, and the dashed black line represents the lower force bound F_L. The values of F_U and F_L are plotted with respect to the wiper's position $\theta \in [0, \pi/2]$. The red lines exemplify feasible force functions of $F_s(\theta)$. The maximum and the minimum allowable spring forces is limited at 6.34 N and 3.1 N when $\theta = 0$ and $\theta = \pi/2$ respectively. According to (2), $F_s(\theta = \pi/2) = k\Delta L + F_i$ represents the initial spring force, where $\Delta L \geq 0$. The selection from the infinite feasible spring functions impacts on the eyelid wiper's maximum attainable actuation cycle that will be investigated in Section V-C.

Fig. 3b-f show how the force bounds F_U and F_L change with respect to various values of $N, r_1/r_2, d, r_3/r_2, F_N$. The parameters $N, r_1/r_2, d$ are related to the force of SMA wires in (1) and (3). Therefore, the increasing of these parameters $N, r_1/r_2, d$ shifts the force bounds towards higher values. In contrast, the parameters r_3/r_2 and F_N impact on the term of the frictional force. The increasing and decreasing of these parameters will lead to the narrowing and expanding of the region between F_U and F_L respectively.

By determining $F_s(\theta = 0)$ and $F_s(\theta = \pi/2)$, a compatible micro extension spring can be designed with the aid of Advance Spring Design software (Universal Technical Systems, Inc.) according to the desired external diameter, music wire diameter, and body length of the spring.

C. Actuation Cycle Analysis

Recognizing the infinite combinations of feasible spring parameters for the SMA actuator, we investigate how different spring parameters impact on the actuation cycle of the eyelid wiper by using the actuation cycle model developed in Section IV.

To conduct the analysis, the parameters involved in the actuation cycle model are presented in Table II according to our initial prototype design in Section V-D. The polynomial parameters in (14) and (15) are computed as $p_1 = 122.63, p_2 = 28.97, p_3 = 0.0098, q_1 = -1165.1, q_2 = -82.67, q_3 = -0.455, q_4 = 1$. Based on the identified parameters in Table I and Table II, five sets of feasible extension spring parameters k, F_i (assuming $\Delta L = 0$) are investigated: (a)-(0.485 N mm^{-1}, 2.75 N),

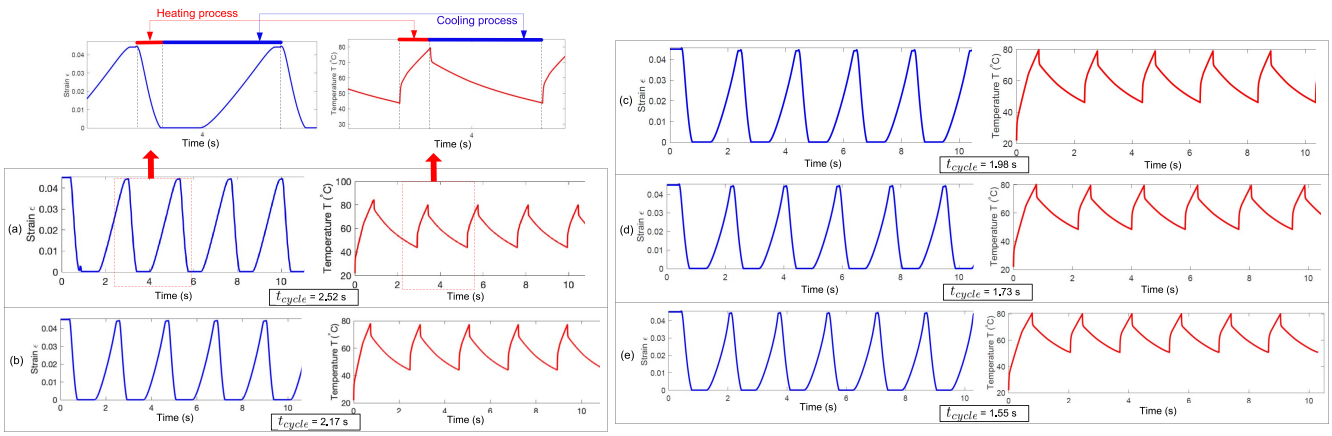

Fig. 4. The predicted cycles of strain and temperature computed by using different spring parameters. (a) $k = 0.485\,\mathrm{N\,mm^{-1}}$, $F_i = 2.75\,\mathrm{N}$. (b) $k = 0.679\,\mathrm{N\,mm^{-1}}$, $F_i = 2.75\,\mathrm{N}$. (c) $k = 0.873\,\mathrm{N\,mm^{-1}}$, $F_i = 2.75\,\mathrm{N}$. (d) $k = 0.485\,\mathrm{N\,mm^{-1}}$, $F_i = 3.25\,\mathrm{N}$. (e) $k = 0.485\,\mathrm{N\,mm^{-1}}$, $F_i = 3.5\,\mathrm{N}$.

(b)-(0.679 N mm^{-1}, 2.75 N), (c)-(0.873 N mm^{-1}, 2.75 N), (d)-(0.485 N mm^{-1}, 3.25 N), (e)-(0.485 N mm^{-1}, 3.5 N). During the heating process, an input current of $I = 1.5\,\mathrm{A}$ was used for Joule heating of SMA wires.

The computed actuation cycles of strain and temperature are demonstrated in Fig. 4. The figures above Fig. 4a show full strain and temperature cycles that include a heating process and a cooling process. In Fig 4a-e, the first cycle takes longer than the following cycles due to the initial temperature $T = T_\infty$ of the SMA wires. During the cycles, the strain of the SMA wires periodically changes between $\epsilon = \epsilon_L$ and $\epsilon = 0$. The actuation cycles $t_{cycle} = t_h + t_c$ vary in Fig. 4a-e because of applying different bias loads. The spring parameters in Fig. 4a-c are set with an identical initial tension $F_i = 2.75\,\mathrm{N}$ and increasing spring rates $k = 0.485\,\mathrm{N\,mm^{-1}}$, $0.679\,\mathrm{N\,mm^{-1}}$, $0.873\,\mathrm{N\,mm^{-1}}$. The actuation cycles are measured as $t_{cycle} = 2.52\,\mathrm{s}$, $2.17\,\mathrm{s}$, and $1.98\,\mathrm{s}$ respectively. While for the spring parameters in Fig. 4a, d, e, the spring rate is kept identical as $k = 0.485\,\mathrm{N\,mm^{-1}}$, and the initial tensions are increased as $F_i = 2.75\,\mathrm{N}$, $3.25\,\mathrm{N}$, and $3.5\,\mathrm{N}$. The actuation cycles are measured as $t_{cycle} = 2.52\,\mathrm{s}$, $1.73\,\mathrm{s}$, and $1.55\,\mathrm{s}$.

According to the numerical analysis, the actuation cycle of the eyelid wiper can be reduced by employing a "stronger" spring within the feasible design region. We also observed that the initial tension F_i has greater influence on the actuation cycle than the spring rate k. The prediction accuracy of the actuation cycle is experimentally evaluated in Section V-D by using the fabricated prototype.

In addition, the parameter Δr used in (10) and specified in Table II is estimated because of the irregular shape of aluminum structure surrounding the SMA wires. We have investigated the values of Δr in the range from 1 mm to 8 mm which yield insignificant influence on the actuation cycle compared with the spring parameters.

D. Prototype Fabrication and Actuation Cycle Evaluation

1) Prototype: Fig. 5 demonstrates a prototype of the vClear system according to the design parameters in Table I and Table II. Fig. 5b shows the appearance of the modularized vClear system, and Fig. 5a shows the integration of the vClear system in the robotic camera as the camera's sealing cover. Fig. 5c illustrates the components of the vClear system that include SMA wires, a cover lens, aluminum structures, a micro extension spring, and a thermistor as described in Section V-A. We purchased off-the-shelf micro extension springs manufactured by using music wires with the parameters shown in Table III. The spring rate is very close to the one evaluated in the case of Fig. 4b. To match the initial tension to 2.75 N as well, we elongate the micro spring with $\Delta L = 3.2\,\mathrm{mm}$ when the eyelid wiper's position is at $\theta = \pi/2$.

The SMA wires are terminated inside the module with the wire leads connecting to a current source. The input current is controlled by using a MOSFET switch and a micro controller.

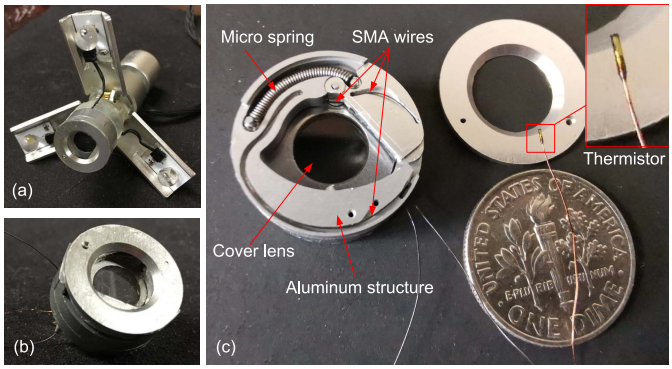

Fig. 5. Prototype of the vClear system. (a) Integrating the vClear system in the robotic camera. (b) The modularized vClear system. (c) Configuration of the vClear system.

TABLE III
MANUFACTURED MICRO EXTENSION SPRING PARAMETERS

Parameters	Value
ϕ_D Outer diameter (mm)	1.2
ϕ_I Inner diameter (mm)	0.76
ϕ_m Music wire diameter (mm)	0.22
k Spring rate (N mm^{-1})	0.669
F_i Initial tension (N)	0.62
L_m Body length (mm)	10.1
ΔL Spring initial extension (mm)	3.2

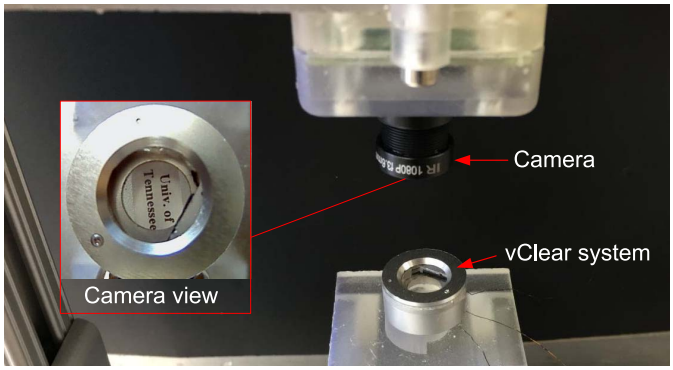

Fig. 6. Experimental platform for recording the actuation cycle of the eyelid wiper, and inspecting the cover lens cleaning efficiency.

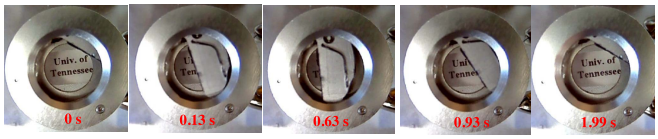

(a) Recorded eyelid wiper motion with time stamps.

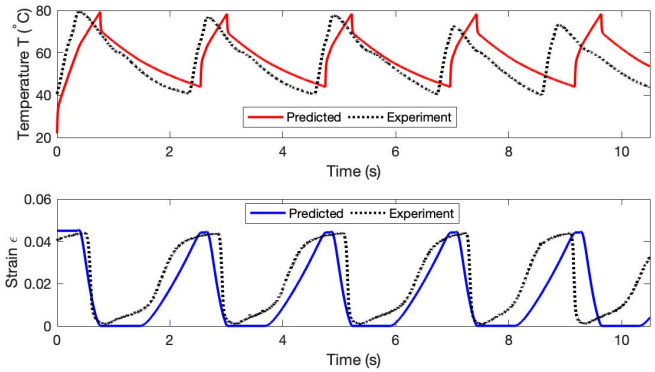

(b) Actuation cycle model validation by experimental data.

Fig. 7. Experimental measurement of actuation cycle for validating the prediction model.

The thermistor connects to the micro controller as well for providing SMA temperature feedback.

2) Actuation Cycle Tests: To validate the actuation cycle model, we developed an experimental platform for measuring the actuation cycle of the manufactured prototype design, as shown in Fig. 6. A camera with 60 FPS (frames per second) is used to record the motion of the eyelid wiper. The modular actuator is held in a fixed position below the recording camera. According to the recorded position θ of the eyelid wiper in each frame, the strain cycles of SMA wires can be computed by using (12).

The results of actuation cycle tests are presented in Fig. 7. Fig. 7a shows the a set of sampled frames with time stamps to demonstrate the motion of the actuated eyelid wiper. Fig. 7b shows the comparison results between the predicted cycles and the measured cycles. Different from the predicted cycles that are consistent in each period, the consistency of measured cycles are influenced by the stability of input current, surrounding air flows, contact between the thermistor and the SMA wires. Therefore, the measured cycle was acquired

(a) Fogging condition.

(b) Bone dusts condition.

(c) Blood condition.

Fig. 8. Cover lens cleaning tests by involving different types of contaminants.

TABLE IV
COVER LENS CLEANING TESTS

	Contamination		
	Fogging	Bone dusts	Blood
Cycle number	1	2	1
Total time (s)	1.93	4.33	2.12

by averaging 30 cycles as $\bar{t}_{cycle} = 2.08\,\text{s}$. Comparing with the predicted actuation cycle $t_{cycle} = 2.17\,\text{s}$, the difference between the predicted and measured cycles is calculated as $|\bar{t}_{cycle} - t_{cycle}|/\bar{t}_{cycle} = 4.81\%$.

E. Contaminant Removal Tests

Three different types of contaminants, i.e., fogging, blood, and bone dusts, were employed to evaluate the cover lens cleaning efficiency of the vClear system. Blood and bone dusts were acquired from a piece of fresh cattle meat attached on a bone. To demonstrate the cover lens clarity, a group of letters ("Univ. of Tennessee") are positioned underneath the cover lens, which are shown in Fig. 6 and Fig. 7a. In this experiment, we counted the required number of actuation cycles for achieving sufficient clarity of the cover lens.

The left figures in Fig. 8a, Fig. 8b, and Fig. 8c demonstrate that the cover lens is contaminated by fogging, bone dusts, and blood respectively. The middle figures show the sweeping motion by the eyelid wiper for removing the contaminants. The right figures show the cleaning results after one or more actuation cycles. The averaged cycle number and cleaning time used by each case are summarized in Table IV. The experiment results indicate that for fogging and blood conditions, only one cycle are generally needed. The measured cleaning time for these conditions are 1.93 s and 2.12 s respectively. For the case of bone dusts, two consecutive cleaning cycles are generally needed in order to remove all the small particles from the cover lens, which took 4.33 s in total.

VI. Discussion

SMA materials possess properties of high power-to-weight ratio, low driving voltages, 4% $\sim$ 8% recoverable strains, and great bio-compatibility, which attract vast attention of researchers to develop novel actuators in medical application [30]. Biomedical devices and surgical robots for minimally invasive surgery are required to be compatible with small body incisions as well as the confined space in body cavities. The critical needs facilitate the development of SMA actuators such as active catheters [31], vascular stents [32], and deformable surgical instruments [33], etc. Compared with piezoelectric materials, the main limitation of SMA actuators is their significant lower actuation frequencies (0.01 Hz$\sim$ 35 Hz [23]). The actuation frequencies of SMA actuators are determined by the rates of heating and cooling, which are influenced by heat convection/conduction rates, Joule heating strategies, and bias stresses. For many medical applications, the "low actuation frequencies" are sufficient. Research efforts have been made to design SMA actuators with desired actuation frequencies by using active cooling systems [34], [35], employing various Joule heating strategies [36], [37], adopting different bias loads [38]. There is a need for engineers and researchers to know the maximum attainable actuation frequencies by using different combinations of the above design factors before implementing a prototype. The estimation of actuation frequencies of SMA actuators involves analyzing the SMA heat transfer model [39], [40], the SMA constitutive model [24], and SMA phase transformation kinetic model [26], which establish highly nonlinear relation between the governing parameters stress, temperature and strain. An early work [27] has developed an analytical model to investigate SMAs' temperature cycles with different cooling conditions. However, this work simplifies the model by using zero-stress condition that is inapplicable to analyze SMA actuators.

In addition to contribute an innovative modularized vClear system for the visual clarity of fully insertable surgical cameras, another major contribution of this work is the development of an effective numerical model for predicting the actuation cycles of SMA actuators with extension springs as bias loads. According to the developed model, the bias load can be extended to other types, such constant springs/weights, and magnetic coupling forces, etc. The broader impact of this research is that the model can serve as a design tool to assist researchers with predicting actuation frequencies of various SMA actuator designs. Moreover, the vClear system can also be integrated in other surgical robots such as da Vinci SP [41] and Titan Medical's SPORT surgical system [42] with minor modifications.

VII. Conclusion

In the current surgical theatre for minimally invasive surgery, surgeons rely on the visual guidance of laparoscopic cameras to manipulate surgical instruments to carry out surgical procedures. Uninterrupted and clear visual guidance is critical to the success of all these surgeries. However, clarity of the visual field of surgical scope cameras can easily get impaired by contaminated lenses because of vapor condensation, particle debris, rinsing fluid, and body fluid. This work takes on this critical research challenge to develop a modularized clear vision system for insertable surgical cameras. The core of this design is the development of an eyelid wiper mechanism that is actuated by 1-D SMA wires and reset by an micro extension spring. We propose a design method to determine the compatible parameters of the micro spring according to the configuration of SMA wires.

In order to analyze how different spring parameters influence the actuation cycle of the eyelid wiper, we developed a numerical model to estimate the actuation cycles which demonstrates 95.2% prediction accuracy compared with our experimental measurements. The experiment tests showed the actuation cycle of the eyelid wiper is about 2 s. The contaminant removal efficiency was also verified by the experimental conditions of fogging, bone dusts and blood. A maximum of two consecutive cycles were required for achieving the clarity of the cover lens, which took 4.33 s in total.

References

[1] B. S. Peters, P. R. Armijo, C. Krause, S. A. Choudhury, and D. Oleynikov, "Review of emerging surgical robotic technology," *Surg. Endoscopy*, vol. 32, no. 4, pp. 1636–1655, Apr. 2018.

[2] T. G. Manning *et al.*, "Laparoscopic lens fogging: Solving a common surgical problem in standard and robotic laparoscopes via a scientific model," *Surg. Endoscopy*, vol. 32, no. 3, pp. 1600–1606, 2017.

[3] N. L. Lawrentschuk, N. E. Fleshner, and D. M. Bolton, "Laparoscopic lens fogging: A review of etiology and methods to maintain a clear visual field," *J. Endourol.*, vol. 24, no. 6, pp. 905–913, 2010.

[4] N. Yong, P. Grange, and D. Eldred-Evans, "Impact of laparoscopic lens contamination in operating theaters: A study on the frequency and duration of lens contamination and commonly utilized techniques to maintain clear vision," *Surg. Laparoscopy Endoscopy Percutaneous Techn.*, vol. 26, no. 4, pp. 286–289, 2016.

[5] G. Schoofs, "A neglected but frustrating ergonomic issue: The thoracoscopic trocar," *Minimally Invasive Therapy Allied Technol. (MITAT) Official J. Soc. Minimally Invasive Therapy*, vol. 13, no. 3, pp. 133–137, 2004.

[6] E. Sutton *et al.*, "Gaze disruptions experienced by the laparoscopic operating surgeon," *Surg. Endoscopy*, vol. 24, no. 6, pp. 1240–1244, 2009.

[7] B. Zheng, D. V. Martinec, M. A. Cassera, and L. L. Swanström, "A quantitative study of disruption in the operating room during laparoscopic antireflux surgery," *Surg. Innov.*, vol. 22, no. 10, pp. 2171–2177, 2008.

[8] D. A. Wiegmann, A. W. Elbardissi, J. A. Dearani, R. Daly, and T. M. Sundt, "Disruptions in surgical flow and their relationship to surgical errors: An exploratory investigation," *Surgery*, vol. 142, no. 5, pp. 658–665, 2007.

[9] D. Kreeft, E. A. Arkenbout, P. W. J. Henselmans, W. R. van Furth, and P. Breedveld, "Review of techniques to achieve optical surface cleanliness and their potential application to surgical endoscopes," *Surg. Innov.*, vol. 24, no. 5, pp. 509–527, 2017.

[10] E. C. Miller, G. Schmitz, and S. M. Smith, "Endoscopic lens cleaner," U.S. Patent 2009/0 105 543, 2009.

[11] M. Schaning, "Laparoscopic lens wipe feature on surgical device shaft or jaw member," U.S. Patent 2014/0 094 650 A1, 2014.

[12] F. Brody, "Minimally invasive lens cleaner," U.S. Patent 2016/0 022 367 A1, 2016.

[13] J. R. Pribanic and B. Brook, "Endoscopic cleaner," U.S. Patent 2009/0 264 703, 2009.

[14] C. O'Prey, C. A. Clark, and A. I. Fleming, "Endoscope wiper blade cleaner," U.S. Patent 9 763 567 B2, 2017.

[15] J. T. Calhoun and J. A. Redan, "Elimination of laparoscopic lens fogging using directional flow of CO2," *J. Soc. Laparoendoscopic Surgeons (JSLS)*, vol. 18, no. 1, pp. 55–61, 2014.

[16] H. Tatsuki *et al.*, "A novel one-step lens cleaning device using air and water flow for endoscopic surgery," *PLoS ONE*, vol. 13, no. 7, pp. 1–9, Jul. 2018.
[17] H. Tada, Y. Omori, K. Hirokawa, H. Ohira, and M. Tomonaga, "Eye-blink behaviors in 71 species of primates," *PLoS ONE*, vol. 8, no. 5, pp. 1–9, 2013.
[18] X. Liu, R. Y. Abdolmalaki, T. Zuo, Y. Guan, G. J. Mancini, and J. Tan, "Transformable *in-vivo* robotic laparoscopic camera with optimized illumination system for single-port access surgery: Initial prototype," *IEEE/ASME Trans. Mechatronics*, vol. 23, no. 4, pp. 1585–1596, Aug. 2018.
[19] A. R. Yazdanpanah, X. Liu, N. Li, and J. Tan, "A novel laparoscopic camera robot with *in-vivo* lens cleaning and debris prevention modules," in *Proc. IEEE/RSJ Int. Conf. Intell. Robots Syst. (IROS)*, Sep. 2017, pp. 3669–3674.
[20] R. J. Wood, E. Steltz, and R. S. Fearing, "Optimal energy density piezoelectric bending actuators," *Sensors Actuators A Phys.*, vol. 119, no. 2, pp. 476–488, 2005.
[21] T. Mirfakhrai, J. D. W. Madden, and R. H. Baughman, "Polymer artificial muscles," *Mater. Today*, vol. 10, no. 4, pp. 30–38, 2007.
[22] A. Miriyev, K. Stack, and H. Lipson, "Soft material for soft actuators," *Nat. Commun.*, vol. 8, no. 1, p. 596, 2017.
[23] S.-H. Song, J.-Y. Lee, H. Rodrigue, I.-S. Choi, Y. J. Kang, and S.-H. Ahn, "35 Hz shape memory alloy actuator with bending-twisting mode," *Sci. Rep.*, vol. 6, Feb. 2016, Art. no. 21118.
[24] C. Liang and C. A. Rogers, "One-dimensional thermomechanical constitutive relations for shape memory materials," *J. Intell. Mater. Syst. Struct.*, vol. 1, no. 2, pp. 207–234, 1990.
[25] K. Tanaka, S. Kobayashi, and Y. Sato, "Thermomechanics of transformation pseudoelasticity and shape memory effect in alloys," *Int. J. Plasticity*, vol. 2, no. 1, pp. 59–72, 1986.
[26] L. C. Brinson, "One-dimensional constitutive behavior of shape memory alloys: Thermomechanical derivation with non-constant material functions and redefined martensite internal variable," *J. Intell. Mater. Syst. Struct.*, vol. 4, no. 2, pp. 229–242, 1993.
[27] A. R. Shahin, P. H. Meckl, J. D. Jones, and M. A. Thrasher, "Enhanced cooling of shape memory alloy wires using semiconductor 'heat pump' modules," *J. Intell. Mater. Syst. Struct.*, vol. 5, no. 1, pp. 95–104, 1994.
[28] J. Butcher, *Numerical Methods for Ordinary Differential Equations*. Chichester, U.K.: Wiley, 2003.
[29] Dynalloy Inc. *Technical Characteristics of Flexinol Actuator Wires*. Accessed: Jul. 19, 2018. [Online]. Available: http://www.dynalloy.com/pdfs/TCF1140.pdf
[30] J. M. Jani, M. Leary, A. Subic, and M. A. Gibson, "A review of shape memory alloy research, applications and opportunities," *Mater. Design (1980–2015)*, vol. 56, pp. 1078–1113, 2014.
[31] B. Konh, S. Karimi, and S. Miller, "Feasibility study of an active soft catheter actuated by SMA wires," in *Proc. SPIE Smart Struct. NDE Ind. 4.0*, 2018, pp. 10602–10605.
[32] G. Mani, M. D. Feldman, D. Patel, and C. M. Agrawal, "Coronary stents: A materials perspective," *Biomaterials*, vol. 28, no. 9, pp. 1689–1710, 2007.
[33] L. Blanc, A. Delchambre, and P. Lambert, "Flexible medical devices: Review of controllable stiffness solutions," *Actuators*, vol. 6, no. 3, p. 23, 2017.
[34] F. Taylor and C. Au, "Forced air cooling of shape-memory alloy actuators for a prosthetic hand," *J. Comput. Inf. Sci. Eng.*, vol. 16, no. 4, 2016, Art no. 041004.
[35] R. A. Russell and R. B. Gorbet, "Improving the response of SMA actuators," in *Proc. IEEE Int. Conf. Robot. Autom.*, vol. 3, 1995, pp. 2299–2304.
[36] Y. H. Teh and R. Featherstone, "A new control system for fast motion control of SMA actuator wires," in *Proc. Shape Memory Related Technol. Conf. (SMART)*, Nov. 2004, pp. 1–13.
[37] P. Motzki, T. Gorges, M. Kappel, M. Schmidt, G. Rizzello, and S. Seelecke, "High-speed and high-efficiency shape memory alloy actuation," *Smart Mater. Struct.*, vol. 27, no. 7, 2018, Art. no. 075047.
[38] W. Huang, "Shape memory alloys and their application to actuators for deployable structures," Ph.D. dissertation, Eng. Dept., Cambridge Univ., Cambridge, MA, USA, 1998.
[39] A. Bhattacharyya, L. Sweeney, and M. G. Faulkner, "Experimental characterization of free convection during thermal phase transformations in shape memory alloy wires," *Smart Mater. Struct.*, vol. 11, no. 3, p. 411, 2002.
[40] S. Huang, M. Leary, T. Ataalla, K. Probst, and A. Subic, "Optimisation of Ni–Ti shape memory alloy response time by transient heat transfer analysis," *Mater. Design*, vol. 35, pp. 655–663, Mar. 2012.
[41] Intuitive Surgical Inc. *DA Vinci SP*. Accessed: Jul. 19, 2018. [Online]. Available: https://www.intuitivesurgical.com/sp/
[42] Titan Medical Inc. *Sport Surgical System*. Accessed: Jul. 19, 2018. [Online]. Available: http://titanmedicalinc.com/technology/#